Received June 7, 2021, accepted June 23, 2021, date of publication June 28, 2021, date of current version July 8, 2021.

Digital Object Identifier 10.1109/ACCESS.2021.3093204

Dual-Polarization and Dual-Band Conical-Beam Array Antenna Based on Dual-Mode Cross-Slotted Cylindrical Waveguide

PABLO SANCHEZ-OLIVARES[1], JOSE LUIS MASA-CAMPOS[2], AND EDUARDO GARCIA-MARIN[2]

[1]Centro de Investigación en Procesado de la Información y Telecomunicaciones, Grupo de Radiación (GR), ETSI Telecomunicación, Universidad Politécnica de Madrid, 28040 Madrid, Spain
[2]Group of Radio-Frequency, Circuits, Antennas and Systems (RFCAS), Department of Electronic and Communication Technologies, Universidad Autonoma de Madrid, 28049 Madrid, Spain

Corresponding author: Pablo Sanchez-Olivares (pablo.sanchezo@upm.es)

This work was supported by the Spanish Government through the Agencia Estatal de Investigación / Fondo Europeo de Desarrollo Regional, Unión Europea (AEI/FEDER, UE,) under Grant TEC2016-76070-C3-1-R and in part under Grant PID2020-116968RB-C32.

ABSTRACT Two designs of conical-beam array antennas are presented for different fifth-generation applications. They are based on slotted cylindrical waveguides and a travelling-wave topology, where the waveguide is used to progressively excite a cross-slot array. A total of 384 cross-slots, formed by transversal and longitudinal slots, are grouped in rings of eight equally-spaced cross-slots. The propagation of TM_{01} and TE_{01} modes in the cylindrical waveguide can provide dual polarization by the independent excitation of transversal and longitudinal slots, respectively. Firstly, a dual linearly-polarized antenna design in the 37-40 GHz band is presented, conforming a high-gain conical-beam pattern. Secondly, a similar antenna design working in the 5G dual-band of 26-30 GHz and 37-40 GHz is also presented. In this last case, transversal and longitudinal slots are designed to radiate at two different frequency bands of 26-30 GHz (vertical polarization) and 37-40 GHz (horizontal polarization), recently assigned for very high-speed 5G applications. The dual-band design has been prototyped by combining 3D-printing and CNC milling techniques to experimentally validate the proposed topology, providing high experimental performance. Directive tilted omnidirectional coverages with peak realized gains around 14 dBi have been obtained, as well as a total efficiency between 83% and 90% for both frequency bands.

INDEX TERMS Antenna arrays, slot antennas, microwave antenna arrays.

I. INTRODUCTION

The fifth generation of mobile communications has been the main subject of study by researchers over the last few years to overcome the technological challenges of the future [1]–[3]. The 5G will support demanding services such as enhanced Mobile Broadband to achieve very high data download rates, Ultra-Reliable and Low Latency Communications [4]–[6]. Design requirements for the associated antennas include highly directional patterns, low losses or higher efficiency. Traditionally, printed antennas have been considered as a good solution for mobile communications in terms of low-cost, lightweight and low profile [7]–[9], while waveguide antennas have been used in satellite applications due to the requirements of low loss and high-power handling [10], [11]. Nevertheless, the 5G New Radio defines a variety of different frequency bands above 20 GHz to obtain wider bandwidths that enable higher data rates. The millimeter-wave band from 24.25 to 52.6 GHz has been recently allocated by the latest 3rd Generation Partnership Project (3GPP) technical standard [12], making available the use of waveguide technology for 5G satellite or terrestrial applications [13]–[15]. Typically, waveguide antennas have been used in radar or satellite communications. Nowadays, these antennas could be considered as well as a cost-effective and high-performance solution for 5G applications in millimeter band, thanks to the progress of additive manufacturing techniques. Complex waveguide antenna designs can be manufactured by 3D printing with

The associate editor coordinating the review of this manuscript and approving it for publication was Giorgio Montisci.

a good tradeoff between low-cost, lightweight and simplicity [16]–[18]. This fact clearly represents an advance compared to traditional CNC milling procedures, reducing costs and enabling a profitable mass production.

In this paper, different high-gain conical-beam array antenna structures are proposed. During the last decades, conical-beam antennas have shown great demand due to the fast development of new generation communications. This kind of antennas can be useful to provide a wide coverage in systems with a tilted line of sight between transmitter and receiver. They have been used in several applications such as remote sensing, satellite or mobile communications. For example, on-board antennas in vehicles for navigation satellite communications or satellite tracking require wide-beam coverage to follow the satellite trajectory over the sky [19]–[22]. Due to the integration of satellite and terrestrial networks in the new 5G system, satellite communications play an important role in the extension of 5G mobile networks to hard-to-reach areas or high-mobility scenarios (such as airplanes or trains). In this context, conical-beam antennas can also be useful in 5G indoor networks or ultra-dense hot spot scenarios in the millimeter-wave frequency band. For example, the high-speed communication network of a sport event in a high-capacity stadium can be covered by placing a high-gain conical-beam antenna on the stadium roof [23], [24].

Millimeter-wave conical-beam antenna designs based on microstrip [25], [26] or Substrate Integrated Waveguide (SIW) technology [27], [28] are attractive due to their low cost and low profile. Other millimeter-wave conical-beam antennas have been proposed as well, such as a circular loop of dipoles [29], circular aperture antennas fed by coaxial probes [30], a spiral shape antenna [31] or a radial line slotted array antenna [32]. Most of the published works related to high-gain conical-beam antennas only provide peak realized gains lower than 8 dBi due to its associated omnidirectional azimuthal radiation pattern. In fact, gain values higher to 10 dBi can be considered a design challenge. To the best of the authors' knowledge, only some few works have achieved a very high-gain performance for conical-beam antennas: a Ka-band omnidirectional high-gain bicone antenna of approximately 12.5 dBi in [33]; an annular planar leaky-wave antenna of 15 dBi in [34]; some conical-beam coaxial horn antenna designs for dual/single band in [35] and a conical-beam parabolic reflector antenna fed by two omnidirectional horns in [22], which obtains a maximum gain of 14.9 dBi. Regarding waveguide technology, a small low-directive omnidirectional circularly polarized antenna was firstly introduced in [36] by the authors for space vehicle communications at 37 GHz. This conformal array was composed of a single ring of cross-slot pairs manufactured by CNC milling on a Cylindrical Waveguide (CW). Later, a linearly polarized slotted array antenna was presented in [14] with directive broadside omnidirectional coverage for 5G communications at 28 GHz. Nevertheless, in this case, the CW requires to be filled with PTFE dielectric to achieve the broadside beam direction. Recently, a similar slotted array on CW at 17 GHz has been published by authors [37], but with two remarkable differences. Firstly, a conical instead of a broadside omnidirectional beam is proposed to improve the coverage. Secondly, 3D printing is used instead of CNC milling in order to significantly reduce manufacturing costs. Both features were introduced in the design aiming to possible commercial applications in cellular communications.

In this paper, an evolution of the antenna in [37] is presented, where several rings of transversal slots were located along the CW surface (without dielectric filler). Such design provided a directive conical-beam radiation with a single linear vertical polarization by the excitation of the waveguide TM_{01} mode. In the present work, longitudinal slots excited by the TE_{01} mode are also included in a dual mode CW. The authors presented in [38] a cross-slot travelling-wave array antenna fed by a square waveguide, where the degenerate fundamental modes TE_{10} and TE_{01} were excited by using an orthomode transducer to achieve dual polarization. Following the same idea, an array of cross-slots capable of radiating with vertical and horizontal linear polarizations is proposed in this work. Each polarization is directly related to either of the two modes excited in the feeding waveguide. Nevertheless, the complexity of this structure is significantly higher than the one presented in [38] because in this occasion two non-orthogonal, high-order modes of the CW with different cutoff frequencies are required. A dual-mode feeder will be designed to excite the TM_{01} and TE_{01} modes with a very high mutual isolation, providing orthogonally-oriented surface currents and consequently dual polarization.

Thus, two different conical-beam antenna topologies are proposed to cover the n257 (26.5-29.5 GHz) and n260 (37-40 GHz) frequency bands identified by the 3GPP for future 5G communications [12]. Firstly, a dual-polarized antenna only for the n260 band (37-40 GHz), where the dual polarization is generated by the excitation of the TM_{01} and TE_{01} modes. In addition, a second design of a dual-band antenna covers both the n257 and n260 frequency bands, where the TM_{01} mode generates vertical polarization for the 26-30 GHz band while the TE_{01} mode generates horizontal polarization for the 37-40 GHz band. This alternative design is not trivial considering the spacing between bands as well as the different propagation constants of the excited modes. One of the two proposed designs will be manufactured and measured to experimentally validate the proposed topology, demonstrating the strength of the additive manufacturing process in millimeter band.

II. SINGLE RADIATING ELEMENT: RING OF CROSS-SLOTS

The single radiating element of the proposed antenna is composed of a ring with N equally spaced cross-slots fed by a CW (Fig. 1(a)). Each cross-slot is formed by a Longitudinal Slot (LS) and a Transversal Slot (TS). Thus, the ring of N cross-slots can be analyzed as a ring of TS (Fig. 1(b)) plus a ring of LS (Fig. 1(c)). The TSs and LSs in each ring will be independently excited by different propagation

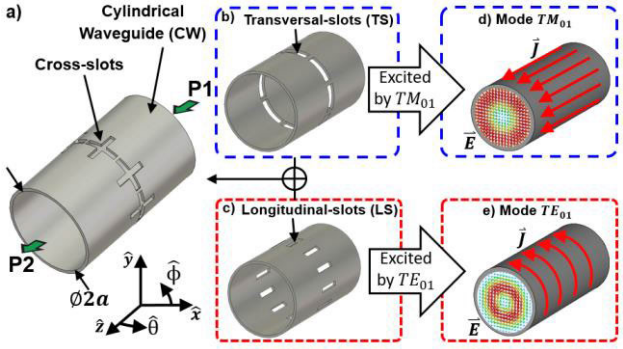

FIGURE 1. Single radiating element: a) Ring of N cross-slots fed by CW; b) ring of N transversal-slots; c) ring of N longitudinal-slots; surface current ($\vec{J}$) and E-field ($\vec{E}$) distribution for modes d) TM_{01} and e) TE_{01}.

modes of the CW. The TM_{01} mode generates longitudinal surface currents on the metallic walls of the CW (following the z-axis, as in Fig. 1(d)). Therefore, the TS can be uniformly excited and a linearly polarized ($\hat{\theta}$-polarization) omnidirectional pattern with minimum ripple is then generated around the CW profile. In the same way, the LS can be excited by the rotational surface current generated by the TE_{01} mode (following the ϕ-axis, as in Fig. 1(e)). Then, an omnidirectional pattern with linear horizontal polarization ($\hat{\phi}$-polarization) is achieved. The propagating modes TM_{01} and TE_{01} generate orthogonal surface currents on the metallic walls of the CW. As a consequence, LS and TS will be fed by orthogonally-oriented currents, and thus the single radiating element (a ring of N cross-slots) can be independently characterized as two rings of N-element TS and N-element LS.

The single radiating element will be characterized for the two different subbands recenctly defined for 5G communications: the 26-30 GHz and the 37-40 GHz frequency bands. This characterization will be essential to perform the conical-beam array antenna designs proposed in Section III. Then, a 2-port unit cell composed of a ring of N equally spaced TS (as in Fig. 1(b)) and a ring of LS (as in Fig.1(c)), both fed by a CW, will be analyzed by *CST Microwave Studio* (*CST*). The radius of the CW is set to $a = 7.1\ mm$ to properly excite the TM_{01} and TE_{01} modes. There are many design criteria to determine the CW radius. However, in this case, it has been selected to adjust the cut-off frequencies of the propagating modes, to optimize the input matching of the single element and to achieve a maximum ripple of 3 dB in the omnidirectional pattern. The CW with a radius of $a = 7.1\ mm$ can propagate seventeen modes up to 40 GHz (where the TM_{01} and TE_{01} modes are the third and sixth modes, respectively). Nevertheless, as it will be shown in Section IV, the appropriate design of a dual feeder will only excite the two desired non-fundamental modes (TM_{01} and TE_{01}).

The characterization of the single element (ring of cross-slots) will be based on the study of the maximum ripple of the omnidirectional pattern generated by the single element as well as its coupling coefficient (C_{oup}). The maximum ripple is obtained by the difference between the maximum and minimum value of the omnidirectional radiation pattern ($\theta = 90°$ plane, following the axes of Fig. 1(a)). The C_{oup} parameter provides the coupling capability of the element when it is fed by a progressive wave (a parameter previously introduced by the authors in several related works such as [37]–[39]). This parameter is specifically defined as the ratio between the power radiated by the slots and the input incident power to them, as it was established in [eq. (1), 37]. Moreover, the characterization will be performed for different number of slots (N = 6, 7, 8, 10, 12, 16) to find the best antenna performance in terms of coupling capability, omnidirectional pattern ripple, simplicity and ease of fabrication.

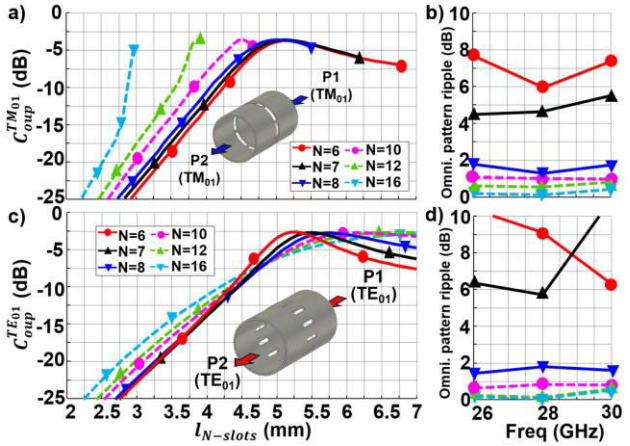

FIGURE 2. Single element characterization at 26-30 GHz for N = 6, 7, 8, 10, 12, 16 slots. Ring of TS excited by TM_{01} mode: a) coupling coefficient (28 GHz) versus slot's length and b) maximum ripple of the omnidirectional pattern versus frequency; Ring of LS excited by TE_{01} mode: c) coupling coefficient (28 GHz) versus slot's length and d) maximum ripple of the omnidirectional pattern versus frequency.

Thus, the entire characterization of the single element for the 26-30 GHz band is presented in Fig. 2. Firstly, Fig. 2(a) shows the coupling coefficient of the ring of N-TS when it is excited by the TM_{01} mode ($C_{oup}^{TM_{01}}$) at 28 GHz. Peak values between -4 and -3 dB have been achieved for all cases, except for N = 16. Nevertheless, the higher N is, the higher the sensitivity of $C_{oup}^{TM_{01}}$ to the slot length ($l_{N-slots}$) variations. Moreover, the larger elements are hardly manufacturable since the wall between slots becomes too thin. Therefore, in order to avoid manufacturing issues, it is preferable to discard N = 12 and N = 16. Following, Fig. 2(b) shows the maximum ripple of the omnidirectional pattern generated by the ring of TS. It must be noticed that the ripple is higher when N is lower. Then, structures with $N < 8$ should be discarded because the maximum ripple is higher than 3-dB. A similar reasoning must be followed for the characterization of the ring of LS. The coupling of this structure (shown in Fig. 2(c)) is denoted as $C_{oup}^{TE_{01}}$ due to the TE_{01} mode excitation of this case. A maximum value around -3 dB is achieved for the coupling coefficient, similar to the ring of TS. The sensitivity of all $C_{oup}^{TE_{01}}$ curves is quite similar, and all analyzed N values

are perfectly manufacturable for the ring of LS. Nevertheless, the maximum ripple values presented in Fig. 2(d) are higher than 3 dB for $N < 8$, so the N = 7 and N = 6 choices are completely rejected.

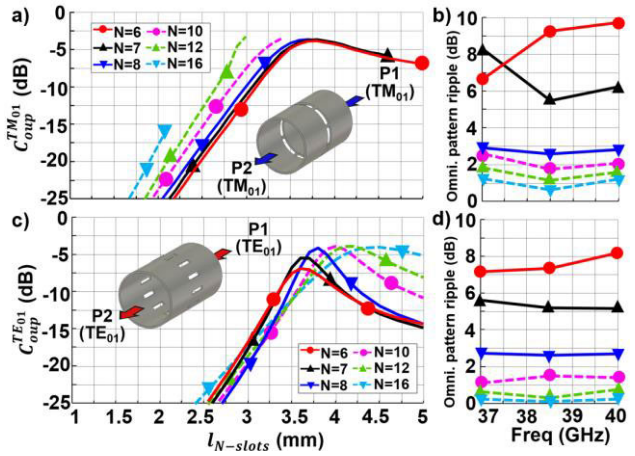

FIGURE 3. Single element characterization at 37-40 GHz band for N = 6, 7, 8, 10, 12, 16 slots. Ring of TS excited by TM_{01} mode: a) coupling coefficient (38.5 GHz) versus slot's length and b) maximum ripple of the omnidirectional pattern versus frequency; Ring of LS excited by TE_{01} mode: c) coupling coefficient (38.5 GHz) versus slot's length and d) maximum ripple of the omnidirectional pattern versus frequency.

On the other hand, Fig. 3 presents for the 37-40 GHz band the same parameters previously shown in Fig. 2 for the other band. In particular, Fig. 3(a) and Fig. 3(b) present the $C_{oup}^{TM_{01}}$ parameter at 38.5 GHz and the omnidirectional pattern ripple in band for the ring of N-TS (exciting the TM_{01} mode), while Fig. 3(c) and Fig. 3(d) show the $C_{oup}^{TE_{01}}$ parameter at 38.5 GHz and the ripple in band for the ring of N-LS (exciting the TE_{01} mode). A similar conclusion than in the previous case can be obtained: a ring of slots with N < 8 will have a maximum ripple higher than 3-dB, while the coupling coefficient of a ring of slots with N > 10 will be too sensitive and hardly manufacturable.

Therefore, according to the previous exhaustive analysis, it was finally decided that the single element is confirmed by N = 8 equally spaced cross-slots to stablish a trade-off between manufacturability (the walls between TS would become too thin for N > 8), low ripple and sensitivity of the coupling capability. For N = 8, the azimuthal distance between slots is equal to $0.54\lambda_0$ at 28 GHz and $0.74\lambda_0$ at 38.5 GHz (λ_0 being the free-space wavelength).

In order to properly characterize the single radiating element, it is essential to demonstrate the isolation between TS and LS. Therefore, the coupling coefficients of the ring of eight cross-slots are presented in Fig. 4 for the excitation of the TM_{01} mode ($C_{oup}^{TM_{01}}$) and the TE_{01} mode ($C_{oup}^{TE_{01}}$) into the feeding CW. Firstly, the coupling parameter is calculated for different TS lengths (l_{8-TS}) and the LS length (l_{8-TS}) is fixed to the resonant value. The results are presented in Fig. 4(a) and Fig. 4(b) for 28 GHz and 38.5 GHz, respectively. The obtained $C_{oup}^{TM_{01}}$ curves are quite similar to the corresponding ones presented in Fig. 2(a) and Fig. 3(a) for N = 8, demonstrating that the presence of the LS does not degrade the coupling capability of the TS. In addition, the $C_{oup}^{TE_{01}}$ remains almost constant, so the variation of the l_{8-TS} has not influence in the coupling capability of LS. This fact is also demonstrated in Fig 4(c) and Fig. 4(d) where the coupling coefficients for 28 GHz and 38.5 GHz are shown, respectively. In this case, the LS lengths (l_{8-LS}) are swept and the TS lengths (l_{8-TS}) are fixed to the resonant value. The obtained $C_{oup}^{TE_{01}}$ curves show a great similarity with the related coupling parameters presented in Fig. 2(a) and Fig. 2(c), also demonstrating a great isolation between TS and LS into the ring of cross-slots element.

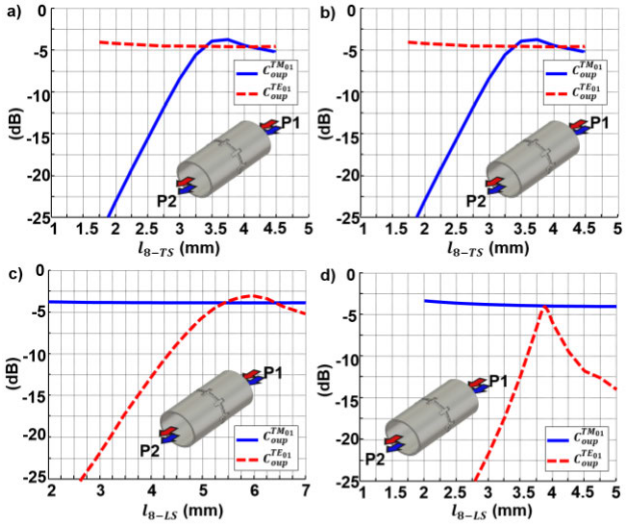

FIGURE 4. Ring of N = 8 cross-slots excited by TM_{01} and TE_{01} modes: a) Coupling coefficients at 28 GHz when l_{N-TS} is swept and l_{N-LS} is fixed to 5.75 mm, b) coupling coefficients at 38.5 GHz when l_{N-TS} is swept and l_{N-LS} is fixed to 3.75 mm, c) coupling coefficients at 28 GHz when l_{N-LS} is swept and l_{N-TS} is fixed to 5.00 mm, d) coupling coefficients at 38.5 GHz when l_{N-LS} is swept and l_{N-TS} is fixed to 3.75 mm.

III. CONICAL-BEAM ARRAY ANTENNA DESIGNS

In this section, two different high-gain conical-beam antennas will be designed: a Dual-Polarized Conical-Beam Array Antenna (DP-CBAA) operating in a single band (37-40 GHz) and a Dual-Band Conical-Beam Array Antenna (DB-CBAA) for the dual-band defined at 26-30 GHz and 37-40 GHz.

A. DESIGN RULES

The two proposed array antennas will be designed following a quite similar process to the one presented in [37], although in this case a dual band and dual polarization performance is provided. Both antenna designs (DP-CBAA and DB-CBAA) will be developed following the antenna topology presented in Fig. 5. It is composed of 48-rings of eight cross-slots each. Uniform amplitude feeding distribution ($a_k = 1$, for $k = 1 : M$, where $M = 48$ is the number of array elements) is applied to achieve maximum directivity. Following the formulation developed by the authors in [eq. (3), 40],

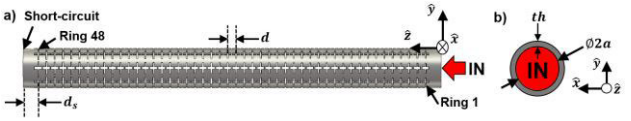

FIGURE 5. Proposed antenna geometry: Conical-beam array antenna fed by a multi-mode CW and conformed by 48 rings of eight cross-slots each.

the required coupling coefficient for each ring k ($C_{oup,k}$) is defined as the ratio between its radiated and incident input powers. Besides, the array is designed to radiate 100% of the total input power. Then, the required $C_{oup,k}$ curve will show the typical ascending tendency of progressive wave antennas. Thus, the slot lengths ($l_{8-slots}^{ring,k}$) must be progressively enlarged as the rings are located further from the antenna input port (as the k index increases). In order to radiate the residual power non-coupled by the slots (100% radiated power), the output port of the CW is loaded by a short-circuit. Then, both the last ring of cross-slots ($k = 48$) and the short must be altogether designed as a matched-load.

Moreover, the distance between elements (in this case, between rings of cross-slots) will be established by the following three main objectives (widely discussed in the design process of [37, Section II]): generate a progressive non-uniform phase difference for both propagated modes in order to obtain a conical-beam radiation pattern, mitigate the grating lobe appearance, and reduce the amplitude of the reflection coefficient at the antenna input port by applying the reflection compensation methodology described in [eq. (6), 40].

B. DUAL-POLARIZED CONICAL-BEAM ARRAY ANTENNA

In this section, the DP-CBAA for the 37-40 GHz frequency band is presented. Considering the design rules described in the previous subsection, the $C_{oup,k}$ parameters required for every ring of cross-slots are presented in Fig 6 (red-curve). Following the single element characterization of Fig. 4(b) and Fig 4(d), the $l_{8-slots}^{ring,k}$ parameters have been set for both LS and TS slots (independently excited by the TE_{01} and TM_{01} modes respectively at the CW input port) in order fulfill the required $C_{oup,k}$ values. On the other hand, the distance between adjacent rings is initially set up to $d = 3.50$ mm.

The slot lengths and ring spacing have been adjusted by an iterative model widely explained by the authors in [39] to compensate mutual coupling effects between adjacent radiating elements. Then, the final TS and LS lengths are represented in Fig. 6(a), demonstrating that LS are slightly longer than TS because the mutual coupling effects are different in both cases. After applying the mutual coupling compensation method, the maximum lengths of the TS and LS are 3.27 mm and 3.70 mm, respectively, while the distance between adjacent rings of slots is fixed to $d = 3.90$ mm $= 0.50\lambda_0 = 0.23\lambda_{g,TM01} = 0.37\lambda_{g,TE01}$ ($\lambda_0$being the free-space wavelength while $\lambda_{g,TM01}$ and $\lambda_{g,TE01}$ are the waveguide wavelengths of the TE_{01} and TM_{01} modes at 38.5 GHz) following the criteria described in Section III.A.

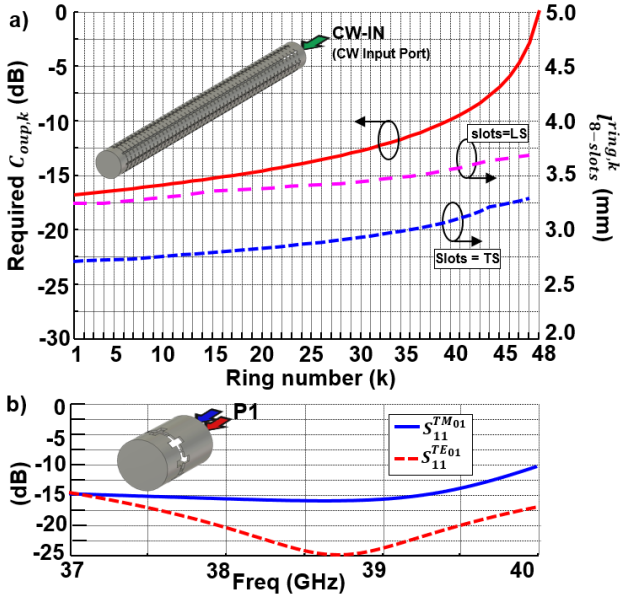

FIGURE 6. Dual-Polarized Conical-Beam Array Antenna (DP-CBAA): a) required coupling coefficients to accomplish a uniform distribution ($C_{oup,k}$) and length of the eight cross-slots for each ring k ($l_{8-slots}^{ring,k}$). b) S-parameters of the last element (48th ring + short) designed as a matched load.

The required coupling coefficient of the last ring of cross-slots ($C_{oup,48}$) is ideally equal to 0 dB because the feeding CW is ended in a short-circuit to radiate the 100% of the input power. Therefore, the last ring of cross-slots and the associated short-circuit are designed as a matched-load structure. The last ring topology and its reflection coefficients for the excitation of TM_{01} and TE_{01} modes are presented in Fig. 6(b). TS and LS lengths are optimized to 4.3 mm and 3.70 mm, while the distance between slots and the short-circuit is $d_s = 6.75$ *mm*. The reflection coefficient is below -10 dB for both cases, demonstrating that most of the residual power is finally coupled and radiated by the last element of the array.

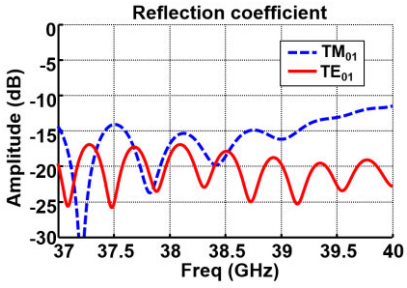

FIGURE 7. Simulated reflection coefficient of the DP-CBAA.

Finally, the DP-CBAA performance has been evaluated by full-wave simulations in *CST*. The reflection coefficient, presented in Fig. 7, is below -11 dB and -16 dB for the excitation of the TM_{01} and TE_{01} modes, respectively. The 3D realized gain radiation patterns at the design frequency (38.5 GHz) corresponding to the TM_{01} and TE_{01} modes excited at

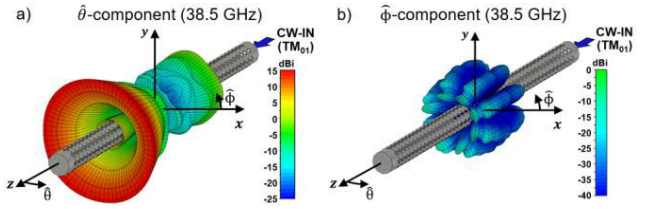

FIGURE 8. Simulated 3D radiation patterns of the DP-CBAA for the excitation of TM_{01} at 38.5 GHz: a) $\hat{\theta}$–component (CP) and b) $\hat{\phi}$–component (XP).

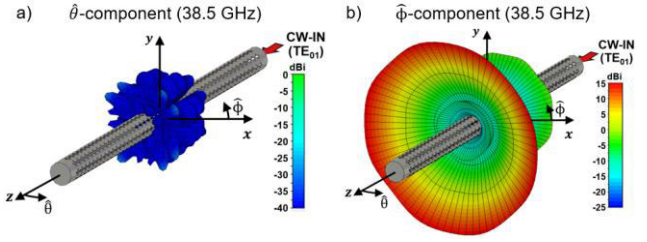

FIGURE 9. Simulated 3D radiation patterns of the DP-CBAA for the excitation of TE_{01} at 38.5 GHz: a) $\hat{\theta}$–component (XP) and b) $\hat{\phi}$–component (CP).

the waveguide input port are shown in Fig. 8 and Fig. 9. In particular, the TM_{01} mode generates the radiated E-field $\hat{\theta}$-component (copolar, CP) and $\hat{\phi}$-component (crosspolar, XP) in Fig. 8(a) and Fig. 8(b), respectively. A conical beam aimed to $\theta = 32$ deg is achieved (58 deg with respect to the xy-plane), with a maximum CP realized gain of 14.8 dBi, while the XP discrimination (XPD, defined as the ratio between CP and XP components) is higher than 20 dB for the main conical-beam. The $\hat{\theta}$-component and $\hat{\phi}$-component presented in Fig. 9(a) and Fig. 9(b) correspond to the XP and CP radiation patterns when the CW of the DP-CBAA is excited by the TE_{01} mode at 38.5 GHz. In this case, the conical beam is pointed to $\theta = 54$ deg, the realized gain peak value of the CP radiation pattern is around 14.5 dBi and the XPD is higher than 30 dB. For both modes, conical-beam performance has been achieved, although with orthogonal linearly polarized radiation. The obtained XPD values ensure a great isolation between these modes. Moreover, the simulated radiation efficiency is higher than 95% at the whole frequency band (37 – 40 GHz) thanks to the use of waveguide technology.

C. DUAL-BAND CONICAL-BEAM ARRAY ANTENNA

In this section, the design of the DB-CBAA is presented. Particularly, TS and LS will operate at 26-30 GHz and 37-40 GHz, respectively (being 28 GHz and 38.5 GHz the design frequencies for each band). For this reason, both the characterization of the ring of TS at 28 GHz (Fig. 4(a)) and the characterization of the ring of LS at 38.5 GHz (Fig. 4(d)) will be used to design the proposed DB-CBAA.

As in the dual polarized antenna of Section III.B, the DB-CBAA is formed by 48 rings of cross-slots. The required $C_{oup,k}$ values as well as the lengths of the TS and LS are presented in Fig. 10(a). By using adequate characterization figures and by applying the mutual coupling compensation method introduced in [39], the length of the slots ($l_{8-slots}^{ring,k}$) are established and optimized. In this design, contrary to the previously presented one in Section III.B, the TS are considerably larger than the LS because their resonant frequency is lower. Thus, TS lengths vary from 4.0 to 5.2 mm while LS lengths vary from 3.2 to 3.75 mm. Moreover, the distance between rings of cross-slots has also been optimized to $d = 3.90$ mm, where $d = 0.30\lambda_{g,TM01} = 0.36\lambda_{01}$ at 28 GHz (λ_{01} and $\lambda_{g,TM01}$ being the free-space and the TM_{01} mode waveguide wavelengths at 28 GHz) and $d = 0.37\lambda_{g,TE01} = 0.50\lambda_{02}$ (λ_{02} and $\lambda_{g,TE01}$ being the free-space and the TE_{01} mode waveguide wavelengths at 38.5 GHz). Finally, the last element (the 48th ring of cross-slots and the short circuit) is also designed as a matched load in this case. The TS and LS lengths are set to 5.22 mm and 3.72 mm, while the distance between the ring and the short-circuit is $d_s = 6.48$ mm. Fig. 10(b) shows that the reflection coefficients of the propagating TM_{01} (at the lower band) and TE_{01} (at the higher band) modes are almost below −10 dB in the whole bands. Therefore, it is demonstrated that the residual power that arrives at the end of the feeding CW is radiated by the last element.

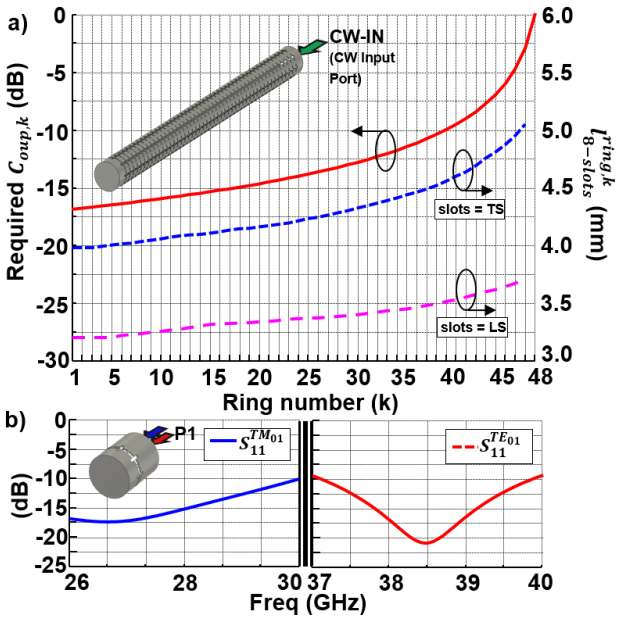

FIGURE 10. Dual-Band Conical-Beam Array Antenna (DB-CBAA): a) required coupling coefficients to accomplish a uniform distribution ($C_{oup,k}$) and length of the eight cross-slots for each ring k ($l_{8-slots}^{ring,k}$). b) S-parameters of the last element (48th ring + short) designed as a matched load.

Thus, full-wave simulation of the DC-CBAA was performed by *CST*. The reflection coefficient of the DB-CBAA has been included in Fig. 11. The reflection is under −20 dB for the 26-30 GHz band when the TM_{01} is excited in the CW input port. Analyzing the higher frequency band (37-40 GHz), the reflection is below −12 dB if the TE_{01} mode is excited. Following, the radiation patterns of

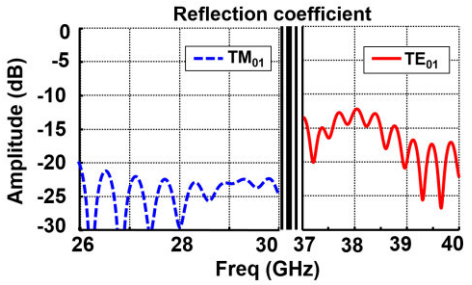

FIGURE 11. Simulated reflection coefficient of the DB-CBAA.

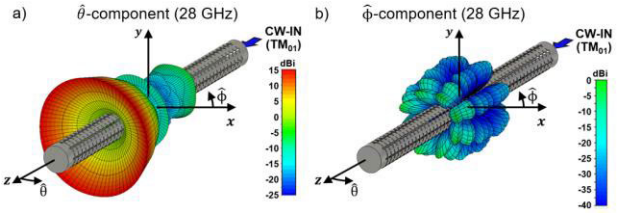

FIGURE 12. Simulated 3D radiation patterns of the DB-CBAA for the excitation of TM_{01} at 28 GHz: a) $\hat{\theta}$–component (CP) and b) $\hat{\phi}$–component (XP).

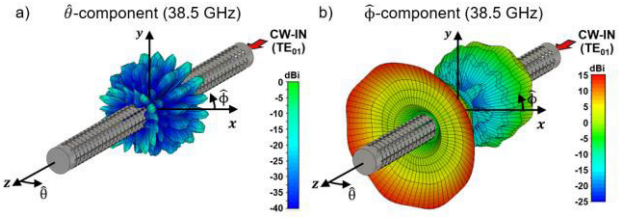

FIGURE 13. Simulated 3D radiation patterns of the DB-CBAA for the excitation of TE_{01} at 38.5 GHz: c) $\hat{\theta}$–component (XP) and d) $\hat{\phi}$–component (CP).

the DB-CBAA have also been simulated by using *CST*. In the first place, the excitation of the TM_{01} mode at the design frequency of the lower band (28 GHz) generates the $\hat{\theta}$-component (CP) and $\hat{\phi}$-component (XP) presented in Fig. 12(a) and Fig. 12(b), respectively. As is shown, a conical beam with a tilted beam of 29 deg from the z-axis, a realized gain of 14.9 dBi and a XPD $>$ 20 dB for the main lobe direction is achieved. Secondly, the $\hat{\theta}$-component and $\hat{\phi}$-component showed in Fig. 13(a) and Fig. 13(b) correspond to the XP and CP radiation patterns when the DB-CBAA is excited by the TE_{01} mode at the design frequency of the higher band (38.5 GHz). In this case, the maximum realized gain value is around 14.2 dBi, the main beam tilt is 38 deg and the XPD is higher than 25 dB. For both frequency bands, the conical-beam performance has been achieved. The main properties of the DB-CBAA (maximum ripple, efficiency, maximum gain, etc…) will be widely analyzed and compared with measurement results in the next section.

IV. INTEGRATION, MANUFACTURING, AND EXPERIMENTAL VALIDATION

In order to experimentally validate the dual-polarized conical-beam antenna topology, the antenna design presented in Section III.C (DB-CBAA) has been selected to be manufactured. The successful fabrication of DB-CBAA, which operates in two bands (28 GHz and 38.5 GHz), will demonstrate the reliability of the method to manufacture this type of topology in these frequency bands. In addition, this fabrication process will also serve to demonstrate that the antenna designed in Section III.B (DP-CBAA), which generates dual polarization in the 38.5 GHz band, can also be satisfactorily manufactured. Before proceeding with the antenna fabrication process, a dual-mode feeder structure will be designed and optimized in order to properly excite the TM_{01} and TE_{01} modes inside the CW. After that, the dual feeder will be integrated with the DB-CBAA, which it will be fabricated by applying additive manufacturing techniques. Finally, the complete antenna structure of the DB-CBAA (slotted CW plus dual-mode feeder) will be measured and analyzed.

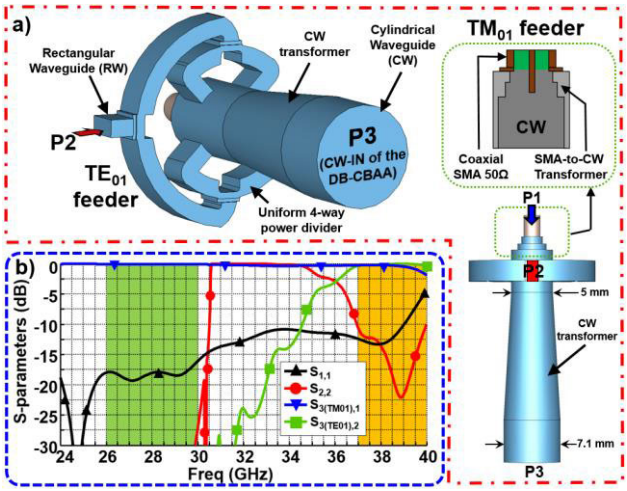

FIGURE 14. Dual-mode and Dual-polarized Feeder (DDF): a) 3-port air model overview and b) simulated S-parameters.

A. DUAL-BAND AND DUAL-POLARIZED FEEDER

A Dual-mode and Dual-band Feeder (DDF) has been designed in order to simultaneously excite the TM_{01} mode at the 26-30 GHz band and the TE_{01} mode at the 37-40 GHz band inside the feeding CW of the DB-CBAA. The feeder is formed by three ports of different propagating topologies, as Fig. 14(a) shows. In particular, the coaxial port 1 is the TM_{01} feeder, the rectangular waveguide port 2 is the TE_{01} feeder, while the CW port 3 is the output connection with the CW input of the slotted antenna (CW-IN of the DB-CBAA in Fig. 10(a)). The TM_{01} mode is excited inside the CW at the lower frequency band (26-30 GHz) by means of a 50Ω-SMA coaxial feeding structure (port 1). A coaxial to CW transition is able to easily excite the TM_{01} mode inside the CW due to the similarity between the E-field distribution of this TM mode in the CW and the TEM mode in the coaxial structure. Then, a two-step circular transformer has been designed and simulated in *CST* to adjust the input matching coefficient for the TM_{01} mode. In addition, the excitation of the fundamental

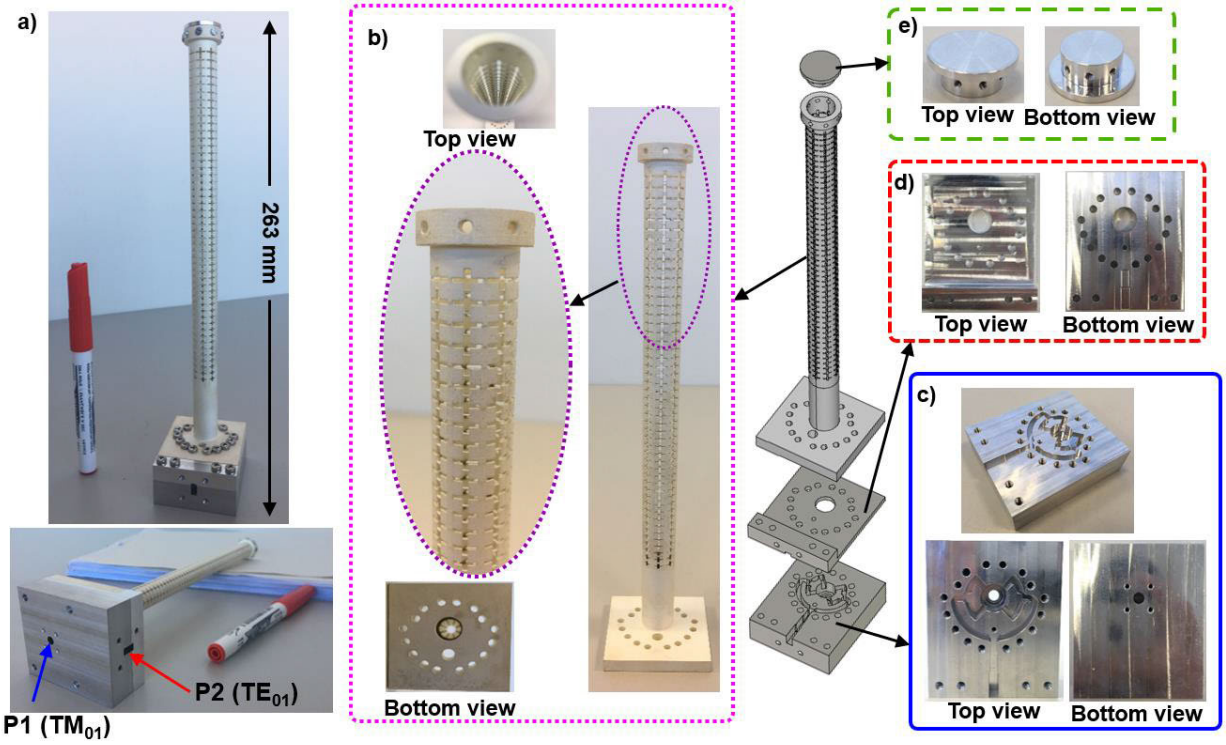

FIGURE 15. DB-CBAA: a) manufactured prototype, b) 3D printed and metallized slotted CW, c) manufactured DDF (lower part), d) manufactured DDF (upper part) and e) mechanized short-circuit.

mode TE_{11} and other higher-order modes are completely avoided by using this transition. On the other hand, the mode TE_{01} is generated at the output CW by the excitation of the fundamental TE_{10} mode in the rectangular waveguide of port 2. A uniform four-way E-plane rectangular waveguide power divider is designed to generate the E-field distribution of the TE_{01} mode in the CW at the corresponding frequency band (37-40 GHz). This kind of TE_{01} feeder has been widely analyzed in other works such as [41], but in our case the structure has been highly compacted. Although a WR-28 standard waveguide has been used at port 2 input, the E-plane power divider has been implemented in a 4.77 mm width and 2.39 mm height waveguide to maximize the input matching of this TE_{01} feeder.

The TM_{01} and TE_{01} feeders are both integrated into the same structure, connecting with a CW section of 5 mm diameter. A simple CW transformer is then introduced in order to match the feeder to the 7.1 mm diameter CW input of the DB-CBAA. Thus, the DDF has been simulated with *CST* and the S-parameters are presented in Fig. 14(b). Firstly, the $S_{x,1}$ parameters refer to the TM_{01} mode excitation of the port 1. As the black-triangle and blue-triangle curves show in the figure, the TM_{01} mode is perfectly generated, both in matching ($|S_{1,1}| < -17$ dB) and transmission terms ($|S_{3(TM01),1}| > -0.2$ dB) from 26 GHz to 30 GHz. However, a matching coefficient $|S_{1,1}| < -7$ dB and a transmission parameter $|S_{3(TM01),1}| > -2$ dB are observed from 37 to 40 GHz. Nevertheless, the radiation efficiency of the DB-CBAA with TM_{01} mode excitation at this band is almost negligible, because the transversal slots have been designed to operate just at the 26-30 GHz band. On the other hand, the TE_{01} mode will only be properly excited in the higher frequency band due to the cut-off frequency of the port 2 rectangular waveguide (31.4 GHz). In this case, the $S_{x,2}$ parameters refer to the port 2 excitation that generates the TE_{01} mode excitation inside the CW-IN of the DB-CBAA. Particularly, the $|S_{2,2}|$ parameter is below -12 dB and the $|S_{3(TE01),2}|$ coefficient is higher than -0.2 dB for frequencies higher than 37 GHz, while the $|S_{3(TE01),2}| < -30$ dB for frequencies lower than 30 GHz. The coupling between modes ($S_{3(TE01),1}$ and $S_{3(TM01),2}$) as well as the isolation between the input ports (S_{21} and S_{12} parameters) are all below -60 dB (not included in Fig. 16(b) for clarity purposes).

B. INTEGRATION AND MANUFACTURING PROCESS OF THE DB-CBAA

The DB-CBAA prototype (Fig. 15(a)) has been implemented by combining several fabrication processes to optimize cost, precision and reliability. Firstly, the slotted CW has been manufactured by means of SLA 3D printing in Protolabs [42] with the Accura Xtreme plastic material and 100 μm thick layer resolution (Fig. 15(b)). This plastic piece has been plated with a 2 μm silver coat by the spray metallization process developed by the company JetMetal [43]. This coating thickness is sufficiently large compared to the skin depth, which is 0.41 μm for silver in the worst case of 24 GHz.

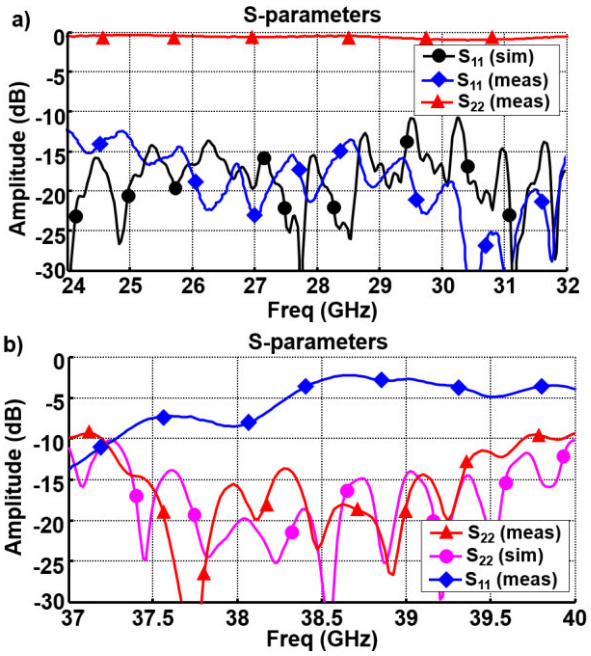

FIGURE 16. DB-CBAA prototype: Simulated and measured S-parameters for the a) lower band (26-30 GHz) and b) higher band (37-40 GHz).

Furthermore, such thickness is in line with common practice in radiofrequency applications such as space communications [44], [45]. Likewise, the JetMetal sprayed metallization shows clear advantages compared to chemical processes such as significant cost cheapening, as well as risk reduction of coating crumbling and peeling.

This DDF is connected to the CW input port of the DB-CBAA. Thus, the TM_{01} and TE_{01} modes are excited into the CW by feeding the ports 1 and 2, respectively. The DDF structure has been fabricated by conventional CNC machining technique in two pieces. The lower part contains the coaxial port 1, the SMA to CW transition and the uniform power divider that generates the TE_{01} mode (Fig. 15(c). The top metallic part (Fig. 15(d)) covers the power divider and implements the WR28 waveguide flange (port 2). Finally, a top metallic cap is also manufactured by conventional CNC milling. This element, located at the end of the slotted CW, is the final short-circuit of the DB-CBAA (Fig. 15(e)).

C. MEASUREMENTS

The DB-CBAA prototype has been measured and compared to the simulations. Firstly, the reflection coefficients for ports 1 and 2 are both analyzed. A good agreement between simulation and measurement curves can be observed. Measured $|S_{11}|$ and $|S_{22}|$ parameters are under -10 dB in Fig. 16(a) for the lower band (26-30 GHz) and in Fig. 16(b) for the higher band (37-40 GHz), respectively. As in the simulated results of the DDF in Fig. 14(b), the lower band will be barely excited by the TE_{01} mode because the S_{22} parameter is higher than -1 dB from 26 to 30 GHz (the cut-off frequency of the TE_{01} mode is 31.4 GHz). Nevertheless, the TM_{01} will be significantly excited in the higher band (37-40 GHz) since the S_{11} parameter is below -3 dB. Despite this fact, it is not considered as an important issue because the power coupled by the TS array could be easily filtered out at port 1. Finally, the isolation between both modes (S_{21} and S_{12}) is below -40 dB (not included in Fig. 16 for clarity purposes).

Following, the normalized directive radiation patterns of the DB-CBAA are presented. In the first place, Fig. 17 shows the radiation patterns at the lower frequency band (26-30 GHz) corresponding to TM_{01} mode excitation of port 1. A comparison between simulations and measurements is presented at $\phi = 0$ deg cutting plane in Fig. 17(a) and at $\phi = 90$ deg in Fig. 17(b). A good agreement between them is reported, which experimentally validates the conical-beam performance of the DB-CBAA. Two tilted main beams at $\theta = \pm 29$ deg are experimentally achieved, with a half power beam-width of 6.4 deg, XPD >16 dB and a Side-Lobe Level (SLL) around -8 dB. This apparently high SLL value is due to the typical lobe increase for a strongly-tilted conical-beam compared to the broadside direction ($\theta = \pm 90$ deg, and SLL ≈ -13 dB for uniform amplitude and phase feeding). On the other hand, a quite similar performance between both cutting planes ($\phi = 0$ deg and $\phi = 90$ deg) has been achieved, demonstrating the revolution symmetry of the conical-beam. Likewise, the typical frequency scanning performance of travelling-wave arrays is also observed in Fig. 17(c). A main beam scanning from ± 33 deg (26 GHz) to ± 26 deg (30 GHz), as well as some changes in the SLL are observed. Secondly, the normalized radiation patterns at the higher frequency band (37-40 GHz) corresponding to the TE_{01} mode excitation (port 2) for the longitudinal slots of the array are presented in Fig. 18. Particularly, Fig. 18(a) and Fig. 18(b) show the simulated and measured patterns at 38.5 GHz for $\phi = 0$ deg and $\phi = 90$ deg cutting planes. Very similar patterns have been obtained for both cases. Two tilted main lobes at $\theta = \pm 38.5$ deg with a narrow beam-width of 3.8 deg are measured, with SLL < -7 dB and XPD > 17 dB. In this case, the main beam scans from ± 40 deg (37 GHz) to ± 37 deg (40 GHz).

In order to evaluate the omnidirectional performance of the conical beam, and to provide an exhaustive analysis of the achieved maximum ripple, the conical radiation patterns in cartesian coordinates are presented in Fig. 19 (lower band, port 1 in Fig. 15(a)) and Fig. 20 (higher band, port 2 in Fig. 15(a)). A reasonable similarity between simulations and measurements can be observed. The maximum variation of the measured patterns is not higher than 1.8 dB from 26 to 30 GHz, while a maximum ripple of 2.1 dB is achieved from 37 to 40 GHz. These performances are consistent with the computed maximum ripple for a ring of eight cross-slots, previously analyzed in the characterization process of the single element of Section II (Fig. 2, Fig. 3 and Fig. 4). Slight tolerance errors in the manufacturing process can be the source of discrepancies between simulations and measurements, as well as the obtained maximum ripple values. Nevertheless, the results can be considered as a high-performance

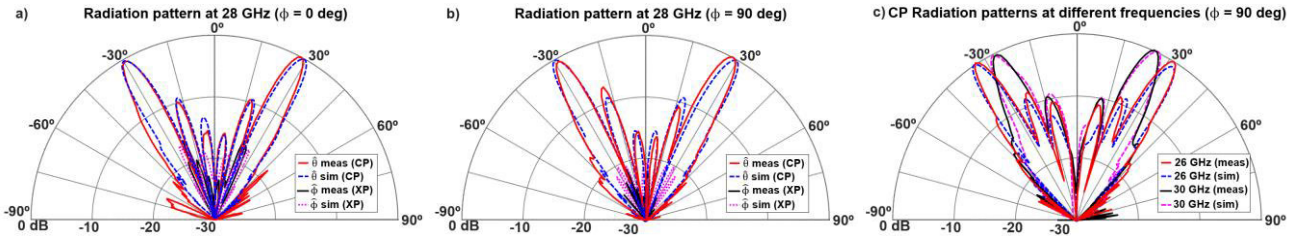

FIGURE 17. DB-CBAA: Comparison between simulations and measurements of the normalized radiation patterns for the excitation of port 1: a) $\phi = 0°$ for 28 GHz, b) $\phi = 90°$ for 28 GHz and c) $\phi = 90°$ for 26 and 30 GHz.

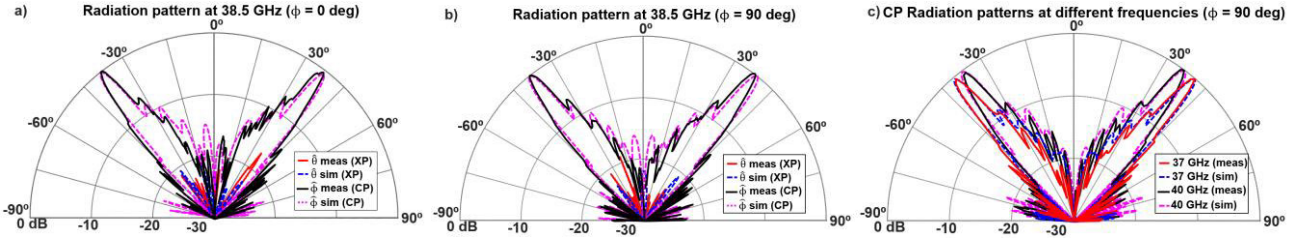

FIGURE 18. DB-CBAA: Comparison between simulations and measurements of the normalized radiation patterns for the excitation of port 2: a) $\phi = 0°$ for 38.5 GHz, b) $\phi = 90°$ for 38.5 GHz and c) $\phi = 90°$ for 37 and 40 GHz.

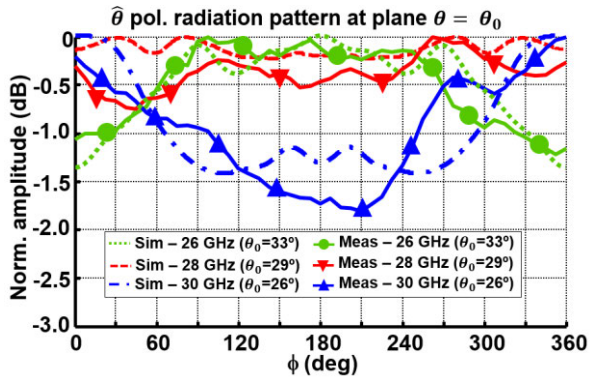

FIGURE 19. DB-CBAA: Simulations and measurements of the normalized conical-beam patterns (26-30 GHz). Excitation of port 1.

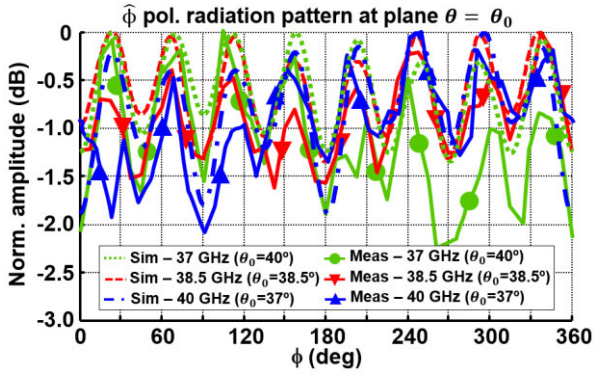

FIGURE 20. DB-CBAA: Simulations and measurements of the normalized conical-beam patterns (37-40 GHz). Excitation of port 2.

omnidirectional pattern for both frequency bands, under a criterion of maximum permitted ripple below 3 dB.

Finally, an analysis of some radiating properties of the DB-CBAA at the main lobe angle for the 26-30 GHz band (Fig. 21) and the 37-40 GHz band (Fig. 22) is provided. Specifically, the maximum values of the simulated directivity (D_{sim}), simulated realized gain (G_{sim}), measured realized gain (G_{meas}) and simulated total efficiency (ε_{sim}, calculated as G_{sim}/D_{sim}) are presented for the two operating bands. Moreover, the parameter named as gain ratio (G_{ratio}, calculated as G_{meas}/G_{sim}) has been defined in order to provide a figure of merit related to the quality of the manufacturing process. In addition, although the directivity parameter could not be measured, the total measured efficiency (ε_{tot}) can be estimated as $\varepsilon_{tot} = G_{meas}/D_{sim}$ considering the good pattern agreement between simulations and measurements.

As Fig. 21 and Fig. 22 demonstrate, quite similar results have been achieved for both frequency bands. The D_{sim} and G_{sim} curves show a great stability for both frequency bands (the gain variation for each curve is around 0.7 dB), with D_{sim}ranging from 14.3 to 15.2 dBi and G_{sim} between 13.8 and 15.0 dBi. Slight differences under 0.4 dB are observed between D_{sim} and G_{sim}. For this reason, the simulated total efficiency ε_{sim} is higher than 90% for both bands thanks to the use of the metallic air-filled waveguide technology. On the other hand, the maximum gain drop between the measured (G_{meas}) and the simulated (G_{sim}) curves is not higher than 0.4 dB, which means that the G_{ratio} is also higher than 90% for both frequency bands. This is a very satisfactory indicator of the manufacturing process.

Finally, the total efficiency ε_{tot} varies (also calculated by the product of ε_{sim} and G_{ratio}) from 86% to 91.5% for the lower band, and between 83% and 90.5% for the higher band. These efficiency values of the proposed DB-CBAA can be considered as remarkable, specially considering the complexity of the antenna topology as well as the manufacturing process based on 3D printing. In this context, the obtained gain ratio between simulation and measurement

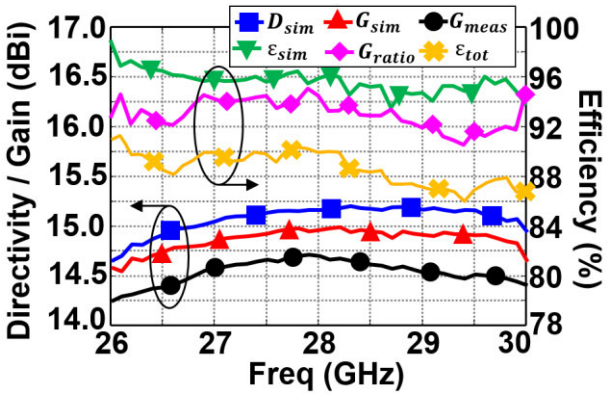

FIGURE 21. DB-CBAA radiating parameters for the excitation of port 1 in the 26-30 GHz band.

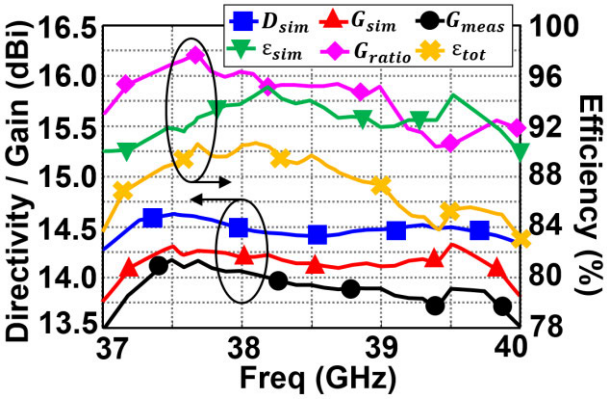

FIGURE 22. DB-CBAA radiating parameters for the excitation of port 2 in the 37-40 GHz band.

($G_{ratio} > 90\%$) clearly demonstrates the suitability of the plastic SLA 3D manufacturing of the company Protolabs in combination with the spray metallization process of the company JetMetal at these frequency ranges.

D. RESULTS DISCUSSION

A comparison with similar works based on high-gain conical-beam antennas operating at 5G-eligible frequencies is summarized in Table 1 to assess the experimental results of the proposed prototype. The antenna presented in this paper outstand as the only with dual-band operation and different polarization in each band. This way, two simultaneous communication channels can operate within the proposed antenna with very low mutual interference, thanks to the frequency and polarization diversity. Other works such as [35], where a coaxial horn antenna is presented, operate in dual/single band but dual polarization is not provided. Furthermore, the impedance bandwidth and radiation pattern results are in line with the values observed in similar works.

Regarding the antenna volume, the proposed antenna shows a compact diameter but a large longitudinal dimension. Nonetheless, this is also the case in the rest of works in the literature, since a large aperture size is inevitable in order to achieve a high gain and thus the conical-beam radiation pattern. For instance, a high-gain access point could be installed in sport venues, where the conical beam would enable a 360 deg. coverage of the stadium bleachers [24]. In any case, despite the considerable antenna size, end user usage could be envisaged when possible. For instance, a reasonable possibility would be the installation of the conical-beam antenna on a vehicle, thus able of establishing communication with satellite links [22].

TABLE 1. Comparison between High-Gain Conical-Beam Antennas.

	[33]	[35]	[22]	[24]	This work
Antenna type	Bicone	Horn	Reflector	Slotted array	Slotted array
Polarization	Single	Single	Single	Single	Dual
Central freq. (GHz)	28.2	10/35 (Dual)	24	26.2	28/38.5 (Dual)
-10 dB Bandwidth (%)	14.2	12.5/8.5	11.3	6.15	14.3/7.8
Max. realized gain (dBi)	12.5	8.8/11.2	14.9	12.1	14.5/14.2
Omnidirectional Ripple (dB)	<1.0	No data	No data	1.3	< 2.1
Total Efficiency	Medium*	High*	Low (30-50%)	High*	High (>83%)
Volume	$\varnothing 33\lambda_0 \times 12.14\lambda_0$	$\varnothing 6.8\lambda_0 \times 5.9\lambda_0$**	$\varnothing 36.7\lambda_0 \times 24\lambda_0$	$\varnothing 0.9\lambda_0 \times 10.6\lambda_0$	$\varnothing 0.96\lambda_0 \times 33.7\lambda_0$**

* Not provided. Estimated.
** λ_0 is the free-space wavelength for the higher band.

Besides, the 3D-printed fabrication of the design in this paper provides a lightweight, low-cost solution for high-speed communications, compared to more complex metal-based alternatives like reflectors or bicone antennas. This way, an affordable mass deployment of the proposed antenna can be envisaged. In addition, the replacement of malfunctioning units can be realized straightforwardly thanks to the low-cost and easy fabrication process.

V. CONCLUSION

In this article, a high-gain conical-beam array antenna design based on a slotted cylindrical waveguide topology is presented. The array antenna is formed by rings of equally spaced cross-slots. The longitudinal and transversal slots that form the cross-slot elements are independently excited by different propagating modes inside the waveguide. In this sense, orthogonal dual linear polarizations are generated in the associated radiation patterns. In particular, the TM_{01} mode generates vertical polarization while the TE_{01} mode generates horizontal polarization. By implementing this topology, two array antenna designs with different properties have been detailed to cover the 26-30 GHz and 37-40 GHz subbands, recently assigned for 5G applications. In the first case, a dual-linearly polarized conical-beam antenna is designed to operate in the 37-40 GHz band. Secondly, the longitudinal and transversal slots are designed to operate at the 26-30 GHz

and 37-40 GHz bands, defining a dual-band conical-beam antenna. The last design has been manufactured in plastic material by 3D printing, and later plated by metallic pulverization, in order to validate the proposed antenna topology and the manufacturing process. A conical-beam pattern, realized gains higher than 13.5 dBi as well as total efficiencies between 83% and 90% have been experimentally achieved for both frequency bands. Therefore, the final prototype can be considered as a high-performance conical-beam antenna in terms of gain, efficiency, low-cost and lightweight, suitable for 5G high data rate communications.

REFERENCES

[1] C.-X. Wang, J. Bian, J. Sun, W. Zhang, and M. Zhang, "A survey of 5G channel measurements and models," *IEEE Commun. Surveys Tuts.*, vol. 20, no. 4, pp. 3142–3168, Aug. 2018.

[2] A. Ghosh, A. Maeder, M. Baker, and D. Chandramouli, "5G evolution: A view on 5G cellular technology beyond 3GPP release 15," *IEEE Access*, vol. 7, pp. 127639–127651, 2019.

[3] S. Sevgican, M. Turan, K. Gokarslan, H. B. Yilmaz, and T. Tugcu, "Intelligent network data analytics function in 5G cellular networks using machine learning," *J. Commun. Netw.*, vol. 22, no. 3, pp. 269–280, Jun. 2020.

[4] M. Benisha, R. T. Prabu, and V. T. Bai, "Requirements and challenges of 5G cellular systems," in *Proc. 2nd Int. Conf. Adv. Electr., Electron., Inf., Commun. Bio-Inform. (AEEICB)*, Chennai, India, Feb. 2016, pp. 251–254.

[5] A. Al-Dulaimi, X. Wang, and I. Chih-Lin, "Machine-type communication in the 5G era: Massive and ultrareliable connectivity forces of evolution, revolution, and complementarity," in *Proc. 5G Netw., Fundam. Requirements, Enabling Technol., Oper. Manage.*, 2018, pp. 519–542.

[6] S. Henry, A. Alsohaily, and E. S. Sousa, "5G is real: Evaluating the compliance of the 3GPP 5G new radio system with the ITU IMT-2020 requirements," *IEEE Access*, vol. 8, pp. 42828–42840, 2020.

[7] S.-Y. Lin and K.-C. Huang, "A compact microstrip antenna for GPS and DCS application," *IEEE Trans. Antennas Propag.*, vol. 53, no. 3, pp. 1227–1229, Mar. 2005.

[8] T. Zhang, R. Li, G. Jin, G. Wei, and M. M. Tentzeris, "A novel multiband planar antenna for GSM/UMTS/LTE/Zigbee/RFID mobile devices," *IEEE Trans. Antennas Propag.*, vol. 59, no. 11, pp. 4209–4214, Nov. 2011.

[9] P. A. Dzagbletey and Y.-B. Jung, "Stacked microstrip linear array for millimeter-wave 5G baseband communication," *IEEE Antennas Wireless Propag. Lett.*, vol. 17, no. 5, pp. 780–783, May 2018.

[10] G. Han, B. Du, W. Wu, and B. Yang, "A novel hybrid phased array antenna for satellite communication on-the-move in Ku-band," *IEEE Trans. Antennas Propag.*, vol. 63, no. 4, pp. 1375–1383, Apr. 2015.

[11] W. Yuan, X. Liang, L. Zhang, J. Geng, W. Zhu, and R. Jin, "Rectangular grating waveguide slot array antenna for SATCOM applications," *IEEE Trans. Antennas Propag.*, vol. 67, no. 6, pp. 3869–3880, Jun. 2019.

[12] *Technical Specification Group Radio Access Network; NR; User Equipment (UE) Radio Transmission and Reception; Part 2: Range 2 Standalone (Release 16)*, document TS 38.101-2, 3GPP, V16.4.0., Jun. 2020. [Online]. Available: https://www.3gpp.org

[13] I. F. da Costa, S. A. Cerqueira, and D. H. Spadoti, "Dual-band slotted waveguide antenna array for adaptive mm-wave 5G networks," in *Proc. 11th Eur. Conf. Antennas Propag. (EUCAP)*, Paris, France, Mar. 2017, pp. 1322–1325.

[14] A. C. Sodré, I. F. da Costa, R. A. dos Santos, H. R. D. Filgueiras, and D. H. Spadoti, "Waveguide-based antenna arrays for 5G networks," *Int. J. Antennas Propag.*, vol. 2018, pp. 1–10, Jan. 2018.

[15] S. Shad, S. Kausar, and H. Mehrpouyan, "Waveguide-fed lens based beam-steering antenna for 5G wireless communications," in *Proc. IEEE Int. Symp. Antennas Propag. USNC-URSI Radio Sci. Meeting*, Atlanta, GA, USA, Jul. 2019, pp. 1149–1150.

[16] M. García-Vigueras, E. Menargues, T. Debogovic, E. Rijk, and J. R. Mosig, "Cost-effective dual-polarised leaky-wave antennas enabled by three-dimensional printing," *IET Microw., Antennas Propag.*, vol. 11, no. 14, pp. 1985–1991, Nov. 2017.

[17] E. Garcia-Marin, J. L. Masa-Campos, P. Sanchez-Olivares, and J. A. Ruiz-Cruz, "Evaluation of additive manufacturing techniques applied to Ku-band multilayer corporate waveguide antennas," *IEEE Antennas Wireless Propag. Lett.*, vol. 17, no. 11, pp. 2114–2118, Nov. 2018.

[18] I. Agnihotri and S. K. Sharma, "Design of a 3D metal printed axial corrugated horn antenna covering full Ka-band," *IEEE Antennas Wireless Propag. Lett.*, vol. 19, no. 4, pp. 522–526, Apr. 2020.

[19] H. Kawakami, G. Sato, and R. Wakabayashi, "Research on circularly polarized conical-beam antennas," *IEEE Antennas Propag. Mag.*, vol. 39, no. 3, pp. 27–39, Jun. 1997.

[20] M. Vicente-Lozano, G. Franceschetti, F. J. Ares-Pena, and E. Moreno-Piquero, "Analysis and synthesis of a printed array for satellite communication with moving vehicles," *IEEE Trans. Antennas Propag.*, vol. 50, no. 11, pp. 1555–1559, Nov. 2002.

[21] K. I. Thimothy and T. Soon Hie, "Conical-beam antenna to compensate free space loss at X-band in LEO satellite systems," in *Proc. 4th Int. Conf. Inf., Commun. Signal Process., 4th Pacific Rim Conf. Multimedia*, Singapore, 2003, pp. 1124–1127.

[22] J. Yang, S.-S. Qi, W. Wu, and D.-G. Fang, "A novel high-gain sum and difference conical beam-scanning reflector antenna," *IEEE Access*, vol. 8, pp. 103291–103300, 2020.

[23] C.-X. Mao, M. Khalily, P. Xiao, T. W. C. Brown, and S. Gao, "Planar sub-millimeter-wave array antenna with enhanced gain and reduced sidelobes for 5G broadcast applications," *IEEE Trans. Antennas Propag.*, vol. 67, no. 1, pp. 160–168, Jan. 2019.

[24] H. R. D. Filgueiras, I. F. da Costa, A. Cerqueira, J. R. Kelly, and P. Xiao, "A novel approach for designing omnidirectional slotted-waveguide antenna arrays," in *Proc. Int. Conf. Electromagn. Adv. Appl. (ICEAA)*, Cartagena, Colombia, Sep. 2018, pp. 64–67.

[25] K. L. Lau and K. M. Luk, "A wideband circularly polarized conical-beam patch antenna," *IEEE Trans. Antennas Propag.*, vol. 54, no. 5, pp. 1591–1594, May 2006.

[26] X. Bai, X. Liang, M. Li, B. Zhou, J. Geng, and R. Jin, "Dual-circularly polarized conical-beam microstrip antenna," *IEEE Antennas Wireless Propag. Lett.*, vol. 14, pp. 482–485, 2015.

[27] D. Guan, Y. Zhang, Z. Qian, and J. Zhang, "Compact circular polarised SIW array antenna with high gain and conical-beam," *Electron. Lett.*, vol. 51, no. 24, pp. 1962–1964, Nov. 2015.

[28] J. Hu, Y. Li, S. Wang, and Z. Zhang, "Millimeter-wave air-filled slot antenna with conical beam based on bulk silicon MEMS technology," *IEEE Trans. Antennas Propag.*, vol. 68, no. 5, pp. 4077–4081, May 2020.

[29] K. Fan, Z.-C. Hao, Q. Yuan, J. Hu, G. Q. Luo, and W. Hong, "Wideband horizontally polarized omnidirectional antenna with a conical beam for millimeter-wave applications," *IEEE Trans. Antennas Propag.*, vol. 66, no. 9, pp. 4437–4448, Sep. 2018.

[30] S. Qi, W. Wu, D.-G. Fang, and Z. Shen, "Circular aperture antenna with conical beam," *IEEE Antennas Wireless Propag. Lett.*, vol. 10, pp. 211–214, 2011.

[31] J. Dyson and P. Mayes, "New circular-polarized frequency-independent antennas with conical beam or omnidirectional patterns," *IRE Trans. Antennas Propag.*, vol. 9, no. 4, pp. 334–342, Jul. 1961.

[32] G. Chenhu, J. Geng, H. Zhou, J. Li, L. Liu, X. Liang, W. Zhu, R. Jin, and R. W. Ziolkowski, "Truncated circular cone slot antenna array that radiates a circularly polarized conical beam," *IEEE Antennas Wireless Propag. Lett.*, vol. 16, pp. 2574–2577, 2017.

[33] S. Liao, P. Chen, and Q. Xue, "Ka-band omnidirectional high gain stacked dual bicone antenna," *IEEE Trans. Antennas Propag.*, vol. 64, no. 1, pp. 294–299, Jan. 2016.

[34] D. Comite, V. G.-G. Buendia, S. K. Podilchak, D. D. Ruscio, P. Baccarelli, P. Burghignoli, and A. Galli, "Planar antenna design for omnidirectional conical radiation through cylindrical leaky waves," *IEEE Antennas Wireless Propag. Lett.*, vol. 17, no. 10, pp. 1837–1841, Oct. 2018.

[35] S.-S. Qi, W. Wu, and D.-G. Fang, "Dual/single band conical-beam nested horn antennas with dual/single pointing angles," *IEEE Trans. Antennas Propag.*, vol. 60, no. 10, pp. 4911–4915, Oct. 2012.

[36] J. L. Masa-Campos, J. M. Fernández, M. Sierra-Pérez, and J. L. Fernández-Jambrina, "Omnidirectional circularly polarized slot antenna Fed by a cylindrical waveguide in millimeter band," *Microw. Opt. Technol. Lett.*, vol. 49, no. 3, pp. 638–642, Mar. 2007.

[37] P. Sanchez-Olivares, J. L. Masa-Campos, E. Garcia-Marin, and D. Escalona-Moreno, "High-gain conical-beam travelling-wave array antenna based on slotted circular waveguide at Ku-band," *IEEE Trans. Antennas Propag.*, vol. 68, no. 8, pp. 6435–6440, Aug. 2020.

[38] P. Sanchez-Olivares, J.-L. Masa-Campos, E. Garcia-Marin, D. Barrio-Tejedor, and P. Kumar, "Dual-linearly polarized travelling-wave array antenna based on triple plus slots fed by square waveguide," *AEU Int. J. Electron. Commun.*, vol. 119, May 2020, Art. no. 153176.
[39] D. Garcia-Valverde, J. L. Masa-Campos, P. Sanchez-Olivares, B. Taha-Ahmed, and J. Corcoles, "Linear patch array over substrate integrated waveguide for Ku-band," *IEEE Antennas Wireless Propag. Lett.*, vol. 12, pp. 257–260, 2013.
[40] J. L. Masa-Campos, S. Klinger, and M. Sierra-Perez, "Parallel plate patch antenna with internal rectangular coupling patches and TE_{N0} mode excitation," *IEEE Trans. Antennas Propag.*, vol. 57, no. 7, pp. 2185–2189, Jul. 2009.
[41] J. R. Montejo-Garai, I. O. Saracho-Pantoja, J. A. Ruiz-Cruz, and J. M. Rebollar, "High-performance 16-way Ku-band radial power combiner based on the TE_{01}-circular waveguide mode," *Rev. Sci. Instrum.*, vol. 89, no. 3, Mar. 2018, Art. no. 034703.
[42] Protolabs. *Design Guidelines: Stereolithography (SLA)*. Accessed: Feb. 1, 2020. [Online]. Available: https://www.protolabs.com/
[43] Jet Metal Tecnnologies. *Metallization Principle*. Accessed: Mar. 2018. [Online]. Available: http://jetmetal-tech.com
[44] D. A. Sheikh, S. J. Connell, and R. S. Dummer, "Durable silver coating for Kepler space telescope primary mirror," *Proc. SPIE*, vol. 7010, Jul. 2008, Art. no. 70104E, doi: 10.1117/12.789996.
[45] S. Shukla, N. Gomathi, and R. George, "Autocatalytic silver-plating of aluminium radio frequency waveguides with autocatalytic nickel as the undercoat for space applications," *Surf. Topogr., Metrol. Properties*, vol. 2, no. 4, Nov. 2014, Art. no. 045004.

PABLO SANCHEZ-OLIVARES was born in Madrid, Spain, in 1987. He received the degree in telecommunication engineering and the Ph.D. degree from the Universidad Autonoma de Madrid (UAM), Spain, in 2011 and 2018, respectively. From 2018 to 2019, he was worked as an Adjunct Professor with UAM, and a Postdoctoral Researcher Associate with the Universidad de Alcalá de Henares (UAH). Since 2019, he has been an Assistant Professor with the Universidad Politécnica de Madrid (UPM). His current research interests include design, manufacturing, and measurement of planar array antennas, phased array antennas, and waveguide antennas.

JOSE LUIS MASA-CAMPOS was born in Madrid, Spain, in 1974. He received the M.Sc. and Ph.D. degrees in telecommunication engineering from the Technical University of Madrid (UPM), Madrid, Spain, in 1999 and 2006, respectively.

From 1999 to 2003, he developed his professional activity with the Research and Development Department, RYMSA, design of base station antennas for mobile communications systems and satellite antennas, where he directed the Research and Development Department, from 2002 to 2003. From 2003 to 2007, he worked as a Research Collaborator with UPM in the design of array antennas for radar and satellites systems in commercial projects for companies as INDRA or SIEMMENS. In 2005, he joined the Autonoma University of Madrid, as an Assistant Professor, and the Radio Frequency, Circuits, Antennas and Systems (RFCAS) Group, Polytechnic College, as an Assistant Professor, in 2011, and also the Chief of the Antennas Section. His current research interests include active and passive planar array antennas, including design theory, measurements and applications. He is a member of the National URSI Conference Organization Committee and he has been the Technical Chairman of the National URSI 2016 Conference celebrated at Madrid.

EDUARDO GARCIA-MARIN was born in Madrid, Spain, in 1992. He received the M.Sc. degree in telecommunication engineering from the Autonoma University of Madrid (UAM), Spain, in 2016, where he is currently pursuing the Ph.D. degree. His current research interests include passive and active array antennas and evaluation of different manufacturing techniques applied to antennas.